Journal of Materials Chemistry B

RSC Publishing

PAPER

View Article Online
View Journal

Published on 03 July 2013. Downloaded by Korea Institute of Science and Technology / KIST on 30/07/2013 02:23:21.

A highly efficient rare earth metal oxide nanorods based platform for aflatoxin detection†

Cite this: DOI: 10.1039/c3tb20690d

Jay Singh,[a] Appan Roychoudhury,[bd] Manish Srivastava,[c] Pratima R. Solanki,[de] Dong Won Lee,[a] Seung Hee Lee*[a] and B. D. Malhotra*[bd]

The nanostructured rare earth metal oxide (samarium oxide, n-Sm_2O_3) nanorods, prepared using a forced hydrolysis technique, have been electrophoretically deposited (EPD) onto an indium-tin-oxide (ITO) glass substrate. This novel platform has been utilized for co-immobilization of monoclonal antibodies of aflatoxin B_1 (Ab-AFB_1) and bovine serum albumin (BSA) *via* electrostatic interactions for food toxin (AFB_1) detection. Thus prepared n-Sm_2O_3 nanorods have been characterized by X-ray diffraction (XRD), atomic force microscopy (AFM), transmission electron microscopy (TEM), X-ray photoelectron spectroscopy (XPS) and Fourier transform infrared (FTIR) spectroscopic techniques. The results of electrochemical response studies of the BSA/Ab-AFB_1/n-Sm_2O_3/ITO immunoelectrode obtained as a function of aflatoxin concentration reveal a linearity of 10–700 pg mL^{-1}, a detection limit of 57.82 pg mL^{-1} cm^{-2}, a response time of 5 s and a sensitivity of 48.39 μA pg^{-1} mL^{-1} cm^{-2} with a regression coefficient of 0.961. The association constant (K_a) for antigen–antibody interactions obtained is 47.9 pg mL^{-1}, which indicates high affinity of antibodies towards the antigen (AFB_1). The application of n-Sm_2O_3 modified electrode for immunosensor analysis offers a novel platform and efficient strategy for the application of rare earth metal oxide materials in bioelectronics.

Received 15th May 2013
Accepted 2nd July 2013

DOI: 10.1039/c3tb20690d

www.rsc.org/MaterialsB

1 Introduction

Recent years have seen increased research activity on applications of the various rare earth (RE) metal oxides in different fields including materials science, bioscience and biotechnology because of their interesting properties and potential applications.[1–4] This is because RE metal oxides are known to display high surface basicity, fast oxygen ion mobility, efficient charge transfer ability and interesting catalytic behavior. Among the various applications such as bioprobes, drug discovery, medical diagnostics, genetic analysis, and flow cytometry of nanostructured RE metal oxides, the applications to bio-sensing have demanded much attention.[5] Among the various RE metal oxides, samarium oxide (Sm_2O_3) has aroused much interest due to its variable valence properties.[6] Besides this, Sm_2O_3, because of its reasonably high relative permittivity (15–30), good thermal stability, and large conduction band (>2 eV),[10] has been predicted to have applications in solar cells,[7] nanoelectronics,[8] semiconductor gases, gate insulators and biochemical sensors.[9] Engstrom *et al.* have used Sm_2O_3 film as a sensing film to fabricate an ion-sensitive field-effect transistor (ISFET) due to its high dielectric constant (~15) and high thermal stability.[11] The Sm_2O_3 nanocrystals have been found to act as active catalysts for CO hydrogenation and as a C_2-oxygenated compound.[12] Wu *et al.* have recently reported sensing characteristics of high-*k* Sm_2O_3 based electrolyte–insulator–semiconductors for urea detection.[13] To the best of our knowledge, no efforts have yet been made to fabricate biosensors based on RE metal oxide for food toxin detection.

Mycotoxins are the toxic secondary metabolites produced by fungi that readily grow on crops, such as cereals, nuts, dried fruits, and beans during plant growth, harvesting, drying, processing, and storage.[14] Environmental conditions such as insect damage, temperature, and humidity may result in increased infection and toxin accumulation. Although hundreds of fungal toxins are known, a limited number is, however, considered to play an important part in food safety. Among these, aflatoxins are known to be highly toxic and carcinogenic secondary

[a]Department of BIN Fusion Technology and Department of Polymer-Nano Science and Technology, Chonbuk National University, Jeonju, Jeonbuk 561-756, Korea. E-mail: jay_singh143@yahoo.co.in; dlee@jbnu.ac.kr; lsh1@jbnu.ac.kr; Fax: +82-63-270-2341; Tel: +82-063-270-2343

[b]Department of Biotechnology, Delhi Technological University, Shahbad Daulatpur, Main Bawana Road, Delhi 110042, India. E-mail: appan.roychoudhury@gmail.com

[c]Department of Physics, Dehradun Institute of Technology (DIT), School of Engineering, Greater Noida 201308, India. E-mail: 84.srivastava@gmail.com

[d]Department of Science & Technology Centre on Biomolecular Electronics, Biomedical Instrumentation Section, Material Physics and Engineering Division, CSIR-National Physical Laboratory, Dr K. S. Krishnan Marg, New Delhi 110012, India. E-mail: pratimarsolanki@gmail.com; bansi.malhotra@gmail.com; Fax: +91-11-27871023; Tel: +91-11-27294668

[e]Special Centre for Nano Sciences, Jawaharlal Nehru University, New Delhi 110067, India. E-mail: partima@mail.jnu.ac.in

† Electronic supplementary information (ESI) available. See DOI: 10.1039/c3tb20690d

Published on 03 July 2013. Downloaded by Korea Institute of Science and Technology / KIST on 30/07/2013 02:23:21.

metabolites produced by three anamorphic species of the genus *Aspergillus*, *A. flavus*, *A. parasiticus* and *A. nomius*.[15] Among the four major aflatoxins B_1, B_2, G_1, and G_2, aflatoxin B_1 (AFB_1) is the most significantly occurring food toxin and is a potent natural carcinogenic, mutagenic and teratogenic compound. The International Agency for Research on Cancer has classified AFB_1 as a human carcinogen since it has been found to be responsible for human hepatocellular carcinoma.[15,16] The World Health Organization (WHO) classifies AFB_1 as a class 1 carcinogen.[17] The aflatoxins display potency of toxicity, carcinogenicity, and mutagenicity in the order: AFB_1> AFG_1> AFB_2> AFG_2.[18] Due to the ubiquitous presence of AFB_1 in foodstuffs and its potential risk to human health and environment, prompt and accurate detection of this food toxin is urgently required.

The analytical methods currently being used for AFB_1 detection are thin layer chromatography (TLC),[19] liquid chromatography, high-performance liquid chromatography (HPLC),[20] immunechromatography,[21] enzyme-linked immunosorbent assay (ELISA)[22] and electrochemical immunoanalysis.[23] Most of these procedures are time-consuming, highly prone to interferents, and may yield unreliable results for some food and biological samples due to the difficulty in obtaining a clear solution for final measurements. Electrochemical immunoassay methods combined with specific antigen–antibody recognition can perhaps be advantageous for the determination of AFB_1[24] because of their simplicity, low detection limit, specificity, *etc*.[25,26] To obtain a sensitive, compact and stable immunosensor platform, the desired antibodies should be directed in a given orientation on a desired electrode. Many nanostructured materials such as gold and nickel nanoparticles, reduced graphene oxide, multiwalled carbon nanotubes and magnetic nanobeads can be utilized for AFB_1 detection.[26–30]

Compared with spherical nanoparticles, one-dimensional (1-D) nanomaterials have recently received increasing interest due to their unique physical and chemical properties.[31,32] Nanorods with unique catalytic activities and electronic properties have been found to result in improved sensitivity and selectivity of the electrochemical biosensors due to increased electron transfer.[33] This is because these small dimensional structures can perhaps be used for efficient transport of electrons. The large surface area and tunable electron transport of these interesting nanostructured materials due to quantum confinement may perhaps play an important role in the operation of a biosensor.[34] A variety of processes have been proposed for the deposition of thin films of nanomaterials on the conductive electrode surface for the fabrication of electrochemical bio-transducers. Among these, the electrophoretic deposition (EPD) technique is known to yield a uniform, dense and porous film with advantages of reduced processing time and simple experimental design.[27,35] The EPD can be accomplished *via* motion of the charged particles, dispersed in a suitable solvent, towards an electrode under the influence of an applied electric field. In addition, as a wet process, EPD provides easy control of thickness and morphology of the deposited film by tailoring various parameters such as deposition time, applied potential, *etc*.[36]

In this work, we have used a forced hydrolysis method to obtain nanostructured Sm_2O_3 nanorods deposited onto an indium-tin-oxide (ITO) glass substrate *via* the EPD technique and subsequently co-immobilize monoclonal antibodies of aflatoxin B_1 (Ab-AFB_1) and bovine serum albumin (BSA) for AFB_1 (food toxin) detection. This fabricated immunoelectrode exhibits low detection limit, low value of association constant (K_a), fast response time and increased shelf-life.

2 Experimental

2.1 Materials

Samarium(III) nitrate hexahydrate [$Sm(NO_3)_3 \cdot 6H_2O$] and sodium hydroxide (NaOH) were purchased from MERCK (New Delhi, India). Aflatoxin B_1 (AFB_1), anti-aflatoxin B_1 mouse monoclonal antibodies (Ab-AFB_1) and bovine serum albumin (BSA, 98%) were procured from Sigma-Aldrich (USA). The stock solution of AFB_1 was freshly prepared in phosphate buffer (50 mM, pH 7.0) with 10% methanol and aliquoted in different working concentrations (0–700 pg mL^{-1}). Ab-AFB_1 was prepared in phosphate buffer (50 mM, pH 7.0) prior to being used. 0.15 M NaN_3 was added into both these solutions as a preservative and stored at −20 °C when not in use. The bovine serum albumin (BSA, 98%) was freshly prepared (2 mg mL^{-1}) in phosphate buffer (50 mM, pH 7.0) and used as a blocking agent for non-specific binding sites. All other chemicals were of analytical grade and used without further purification. The indium-tin-oxide (ITO) coated glass (Balzers) sheet of resistance 15 W cm^{-1} was used as a substrate for deposition of the desired nanocomposite that worked as the working electrode. All solutions in these studies were prepared using deionised water of resistivity of not less than 18 MΩ cm taken from a Milli-Q water purification system (Milli-Q, USA).

2.2 Synthesis of Sm_2O_3 nanorods

The Sm_2O_3 nanorods were prepared using a forced hydrolysis technique. For this purpose, 100 mM of samarium nitrate [$Sm(NO_3)_3 \cdot 6H_2O$] and 1 M of sodium hydroxide (NaOH) were dissolved in 100 mL of deionized water separately and magnetically stirred for 2 h to obtain clear, transparent, homogeneous solutions. The aqueous solution of NaOH was added dropwise to a pale yellowish solution of samarium nitrate until the pH of the resulting solution reached ~11 and was kept under steady stirring for 5 h at room temperature (25 °C). A pale yellow precipitate of $Sm(OH)_3$ thus obtained was washed several times with deionized water and ethanol until a neutral pH was achieved. The resulting solution was magnetically stirred for 90 min at 90 °C. Then after fast cooling in the cold water, we added 10 mL butanol and centrifuged this solution at 5000 rpm for 3 min. The solution was subsequently filtered, and further washed with deionized water and ethanol 4–5 times to remove all the ionic remnants. The precipitate was then dried at 80 °C for 6 h and was calcined at 500 °C for 6 h to obtain Sm_2O_3 nanorods for further characterization. The proposed reaction mechanism for the formation of pure Sm_2O_3 nanoparticles is shown in eqn (i) and (ii).

$$Sm(NO_3)_3 + 3NaOH \rightarrow Sm(OH)_3\downarrow + NaNO_3 \quad \text{(i)}$$

$$2Sm(OH)_3 \xrightarrow[500\ ^\circ C \text{ for } 6\ h]{\Delta} Sm_2O_3 + 3H_2O \quad \text{(ii)}$$

 This journal is © The Royal Society of Chemistry 2013

Published on 03 July 2013. Downloaded by Korea Institute of Science and Technology / KIST on 30/07/2013 02:23:21.

2.3 Electrophoretic deposition of n-Sm_2O_3/ITO films

Electrophoretic deposition (EPD) was carried out by using a DC battery (BioRad, model 200/2.0). Uniform colloidal suspension of Sm_2O_3 nanorods was prepared in de-ionized water (1 mg mL^{-1}) through vigorous stirring followed by sonication for 1 h prior to EPD. A platinum foil (1 cm × 2 cm) was used as the anode and a hydrolyzed ITO-coated glass plate as the cathode. The two electrodes, placed parallel to each other with a separation of 1 cm, were dipped in the n-Sm_2O_3 colloidal suspension. Optimal conditions for EPD of Sm_2O_3 nanorods onto an ITO coated glass surface (0.25 cm^2) have been found to be 25 mV for 50 s to obtain a uniform, thin and homogeneous n-Sm_2O_3 film that exhibits maximum amperometric current. This n-Sm_2O_3/ITO nanocomposite film was washed with de-ionized water to remove any unbound particles and dried at room temperature (25 °C) for 12 h.

2.4 Fabrication of the immunoelectrode

The optimal amount of freshly prepared solution (10 μL) of Ab-AFB_1 was uniformly spread onto the desired n-Sm_2O_3/ITO electrode surface and kept undisturbed in a humid chamber for about 12 h at 25 °C. The Ab-AFB_1/n-Sm_2O_3/ITO electrode was washed thoroughly with phosphate buffer (50 mM, pH 7.0) to remove any unbound antibodies followed by drying at room temperature (25 °C). The non-specific binding sites of the modified Ab-AFB_1/n-Sm_2O_3/ITO electrode were blocked by using bovine serum albumin (BSA, 98%). 10 μL of freshly prepared BSA solution (2 mg mL^{-1}) was uniformly spread over the Ab-AFB_1/n-Sm_2O_3/ITO electrode and kept overnight in a humid chamber at room temperature (25 °C) followed by washing with phosphate buffer (50 mM, pH 7.0) to remove any unbound biomolecules. The optimal amount of Ab-AFB_1 (10 μL) and BSA (10 μL) to obtain the maximum amperometric current response in PBS (50 mM, pH 6.0, 0.9% NaCl) containing $[Fe(CN)_6]^{3-/4-}$ (5 mM) at 20 mV s^{-1} scan rate was determined using the CV technique (see Fig. S1 and S2 in the ESI†). This fabricated BSA/Ab-AFB_1/n-Sm_2O_3/ITO immunoelectrode was dried and further used for characterization and AFB_1 detection. Fig. 1 shows a stepwise fabrication of the BSA/Ab-AFB_1/n-Sm_2O_3/ITO immunosensor along with the biochemical reaction between AFB_1 and Ab-AFB_1 on the n-Sm_2O_3/ITO electrode surface.

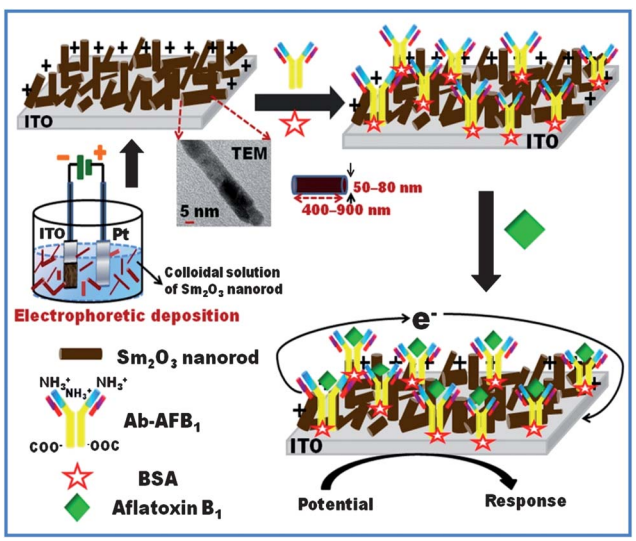

Fig. 1 Schematic illustration of the electrophoretically deposited Sm_2O_3 nanorods and fabrication of the BSA/Ab-AFB_1/n-Sm_2O_3/ITO immunosensor along with the biochemical reaction between AFB_1 and Ab-AFB1.

3 Characterization and measurements

The structure, shape and crystallite size of synthesized Sm_2O_3 nanoparticles have been investigated by X-ray diffraction (XRD) using a Rigaku D/Max 2200 diffractometer with CuKα radiation at $\lambda = 1.5406$ Å. FT-IR spectra of the electrodes have been recorded with a FTIR spectrophotometer (PerkinElmer, Spectrum BX II). Transmission electron microscopy (TEM) studies have been carried out with a JEOL JEM-2200 FS (Japan). The surface morphological studies of n-Sm_2O_3/ITO, Ab-AFB_1/n-Sm_2O_3/ITO and BSA/Ab-AFB_1/n-Sm_2O_3/ITO electrodes have been investigated using atomic force microscopy (AFM, Model VEECO 440, Nanoscope). X-ray photoelectron spectroscopy (XPS) has been performed using an Axis-Nova, Kratos Analytical Ltd., Manchester, UK. The cyclic voltammetry (CV), differential pulse voltammetry (DPV), electrochemical impedance spectroscopy (EIS) and amperometric measurements have been recorded on an Autolab Potentiostat/Galvanostat (Eco Chemie, The Netherlands). The electrochemical measurements have been conducted on a three-electrode system with a BSA/Ab-AFB_1/n-Sm_2O_3/ITO immunoelectrode as the working electrode, a platinum (Pt) wire as the counter electrode, and a saturated Ag/AgCl electrode as the reference electrode in phosphate buffer saline (PBS, 50 mM, pH 7.0, 0.9% NaCl) containing 5 mM $[Fe(CN)_6]^{3-/4-}$ as a mediator.

4 Results and discussion

4.1 XRD and TEM analysis

Fig. 2a illustrates the XRD pattern of the synthesized product. The XRD pattern shows broad diffraction peaks, indicating nanocrystalline nature of the sample. All the diffraction peaks corresponding to (222), (400), (411), (322), (431), (611), (541), (622), and (631) planes are in good agreement with JCPDS-no. 25-0749 and confirm the formation of the cubic structure of the Sm_2O_3 crystal. No peak corresponding to any impurity has been detected, suggesting the single phase of the sample. The average crystallite size calculated by using the Scherrer formula (eqn (iii)) has been found to be ~60 nm.

$$d = \frac{0.9\lambda}{\beta \cos\theta} \quad \text{(iii)}$$

where β is the full width at half maxima (FWHM) of the diffraction peaks, θ is the glancing angle and λ (= 1.54060 Å) is the wavelength of X-ray.

The lattice constant corresponding to the cubic crystal structure of Sm_2O_3 has been calculated to be 10.928 Å using eqn (iv):

$$a = d_{hkl}\sqrt{(h^2 + k^2 + l^2)} \quad \text{(iv)}$$

The size and shape of the Sm_2O_3 nanoparticles have been further investigated using the TEM microscope (Fig. 2b). The

Published on 03 July 2013. Downloaded by Korea Institute of Science and Technology / KIST on 30/07/2013 02:23:21.

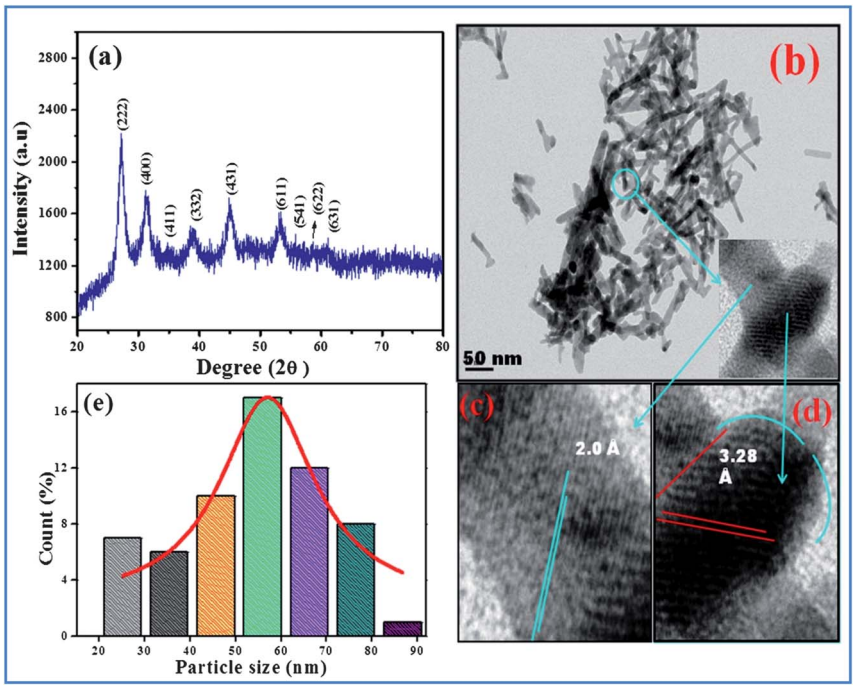

Fig. 2 (a) X-ray diffraction pattern and (b) TEM micrograph. (c and d) HR-TEM micrograph of n-Sm_2O_3 nanorods. (e) Size distribution histograms and Gaussian fits for n-Sm_2O_3 nanorods.

growth of the rod shaped particles can be clearly seen. The individual Sm_2O_3 rod has been selected for HR-TEM analysis (Fig. 2c–d). Lattice fringes with a *d*-spacing of 0.32 nm corresponding to (222) and 0.20 nm corresponding to (431) planes are clearly visible. These observations are in good agreement with *d*-values calculated for the respective planes from the XRD pattern. In order to analyze the size distribution quantitatively the histogram is fitted with the Lorentz function and the mean size of the particle is calculated to be 57 nm (Fig. 2e).

4.2 XPS and FTIR studies

In order to determine the chemical composition of the synthesized product, XPS measurements were also conducted. The wide range XPS survey spectrum of the synthesized sample shown in Fig. 3a indicates no impurities except for carbon as the reference. The deconvoluted Sm3d spectrum (Fig. 3b) consists of two intense bands ~1083.1 eV and 1110.2 eV corresponding to Sm^{3+} and a broad peak with low intensity centred ~1096 attributed to the Sm^{2+} component, suggesting a small amount of oxygen vacancy. The O1s spectrum as shown in Fig. 3c was fitted by three components. A broad peak at ~533.4 eV can be attributed to OH groups, absorbed onto the surface of particles, whereas peaks at ~531.8 eV and ~529.2 eV can be assigned to the oxygen atom of Sm^{3+}–O and Sm^{2+}–O groups, respectively.[32] The coexistence of these peaks reveals the presence of Sm in two different ionic states; therefore, oxygen vacancy in the crystal lattice of Sm_2O_3 is helpful for transferring the charge.

FTIR spectra of the n-Sm_2O_3/ITO, Ab-AFB_1/n-Sm_2O_3/ITO electrode and the BSA/Ab-AFB_1/n-Sm_2O_3/ITO immunoelectrode are shown in Fig. 3d. The IR spectra of the n-Sm_2O_3/ITO film (curve i) exhibits a broad band observed at 3446 cm^{-1} and a small shoulder at 1058 cm^{-1}, corresponding to the O–H stretching and bending vibration of physically absorbed water molecules onto the electrode surface. Two strong absorption peaks observed at 1521 and 1363 cm^{-1} are assigned to rocking and wagging vibration transitions of the O–H group. The appearance of a sharp and intense band at 690 cm^{-1} is assigned to the Sm–O stretching vibration mode revealing the formation of Sm_2O_3 nanoparticles. The Ab-AFB_1 antibodies conjugated with the n-Sm_2O_3/ITO electrode (curve ii) provide increased absorption at 1658 cm^{-1} due to the carbonyl group and a broad strong band observed at 3357 cm^{-1}. However, after immobilization of antibodies, the characteristic peaks containing carbonyl stretching of the amide I band appear at 1654 cm^{-1} and N–H bending of the amide II band at 1562, 1167 and 946 cm^{-1} indicating immobilization of antibodies onto the n-Sm_2O_3/ITO electrode.[26] A broad band seen at 3337 cm^{-1} (O–H stretching vibration) is shifted towards the lower wave number as compared to that of the Ab-AFB_1/n-Sm_2O_3/ITO electrode due to deactivation of the binding sites of Ab-AFB_1. Hence, the Sm–O–Sm inorganic network is bonded with Ab-AFB_1 macromolecules *via* hydrogen bonding as well as electrostatic interactions between antibodies and n-Sm_2O_3 nanoparticles. However, the presence of a 1647 cm^{-1} peak in the spectrum of the BSA/Ab-AFB_1/n-Sm_2O_3/ITO immunoelectrode (curve iii) corresponds to the amide II band of BSA indicating immobilization of BSA on the immunoelectrode.[1] It appears that the immobilized Ab-AFB_1 molecules are favourably oriented when the Fc (carboxyl-terminated group) part is attached to the electrode and its Fab (amino-terminated site) part binds with the desired antigen

 This journal is © The Royal Society of Chemistry 2013

Published on 03 July 2013. Downloaded by Korea Institute of Science and Technology / KIST on 30/07/2013 02:23:21.

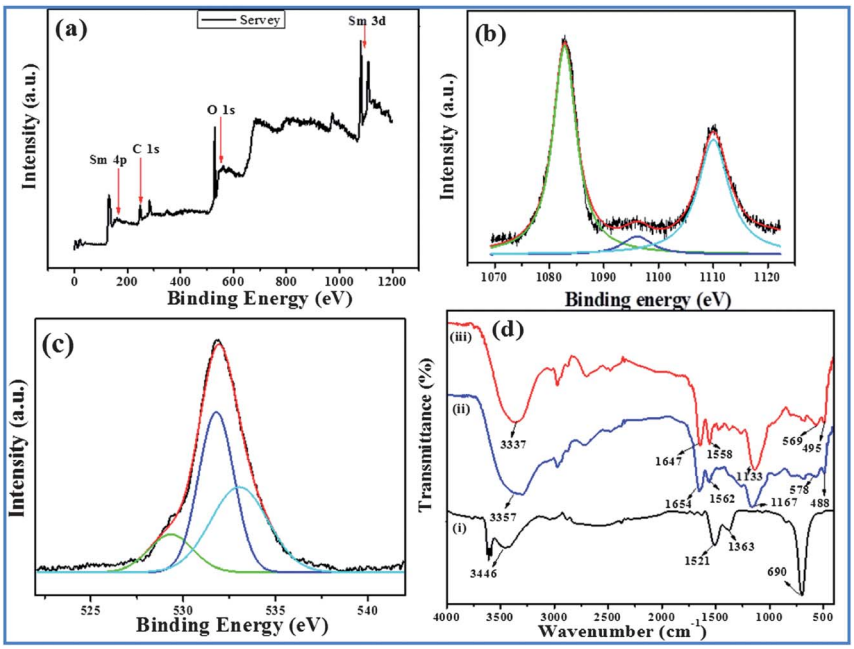

Fig. 3 (a) XPS spectrum of the Sm_2O_3 nanorod calcination at 500 °C for 6 h. (b) The XPS valence-band of Sm3d core level spectra and (c) O1s energy-loss spectrum of the annealed Sm_2O_3 sample. (d) FTIR spectra of n-Sm_2O_3/ITO (i), Ab-AFB_1/n-Sm_2O_3/ITO electrode (ii) and BSA/Ab-AFB_1/n-Sm_2O_3/ITO immunoelectrode (iii).

with a high level of specificity.[1] Fig. 1 shows a schematic of fabrication of the immunosensor and the biochemical reaction of Ab-AFB_1 with AFB_1 at the nanostructured surface. The positively charged n-Sm_2O_3 binds with the carboxyl groups of Ab-AFB_1 *via* electrostatic interactions and the free amino terminal sites of Ab-AFB_1 preferably bind with the carboxylic group of AFB_1 molecules.

4.3 AFM analysis

Surface morphologies of the n-Sm_2O_3/ITO film, Ab-AFB_1/n-Sm_2O_3/ITO electrode and BSA/Ab-AFB_1/n-Sm_2O_3/ITO immunoelectrode have been investigated by atomic force microscopy (AFM) as shown in Fig. 4. The AFM image of the electrophoretically deposited Sm_2O_3 thin film onto the ITO surface (image a) shows the formation of a rough surface with uniformly distributed nanoporous granular morphology. The granular and porous morphology of the n-Sm_2O_3/ITO film changes into regular smooth globular morphology after immobilization of Ab-AFB_1 (image b). This is attributed to immobilization of Ab-AFB_1 *via* an electrostatic interaction between the positive charge (Sm^{3+}) on the n-Sm_2O_3/ITO film and the negative charge of the carboxyl group (COO^-) of the antibody AFB_1. The nanostructured Sm_2O_3 film provides a nanoporous surface resulting in enhanced antibody loading at the Ab-AFB_1/n-Sm_2O_3/ITO electrode surface. However, after immobilization of BSA the surface morphology of the BSA/Ab-AFB_1/n-Sm_2O_3/ITO immunoelectrode (image c) reveals a smoother and even surface due to blocking of non-specific binding sites of the immobilized antibodies. The observed value of Rpm (average max height) increases after immobilization of Ab-AFB_1 (28.3 nm) onto the n-Sm_2O_3 surface, as compared to that of the n-Sm_2O_3/ITO film (16.7 nm), indicating immobilization of the antibodies. The Rpm value further increases for the BSA/Ab-AFB_1/n-Sm_2O_3/ITO immunoelectrode (64.9 nm), which confirms immobilization of the BSA.

4.4 Cyclic voltammetric studies

Fig. 5a shows results of the cyclic voltammetry (CV) studies of the bare ITO, n-Sm_2O_3/ITO electrode, Ab-AFB_1/n-Sm_2O_3/ITO and BSA/Ab-AFB_1/n-Sm_2O_3/ITO immunoelectrode in PBS (50 mM, pH 6.0, 0.9% NaCl) containing $[Fe(CN)_6]^{3-/4-}$ (5 mM) at 20 mV s^{-1} scan rate in the potential range of −0.3 V to 0.6 V. It can be seen that magnitude of the peak current (I_{pa}, 0.28 mA) of the n-Sm_2O_3/ITO electrode (curve ii) is higher than that of the bare ITO electrode (I_{pa}, 0.18 mA, curve i). This is because n-Sm_2O_3 nanorods provide improved electrocatalytic behavior, increased surface area and high surface energy resulting in enhanced electron transport between the medium and the electrode. Moreover, the value of the peak current (I_{pa}, 0.37 mA) further increases after the immobilization of Ab-AFB_1 onto the n-Sm_2O_3/ITO electrode (curve iii). This may be attributed to the available non-binding sites (*i.e.* free NH_3^+ group) onto the Ab-AFB_1 immobilized n-Sm_2O_3/ITO electrode that play an important role resulting in accelerated electron transfer between Ab-AFB_1 and the n-Sm_2O_3/ITO electrode. However, magnitude of the current response (curve iv) decreases after immobilization of BSA due to blocking of the non-specific binding sites of Ab-AFB_1 that hinder the electron transfer between the medium and electrode, indicating immobilization of BSA onto the Ab-AFB_1/n-Sm_2O_3/ITO bioelectrode. The results of the differential pulse voltammetry (DPV) studies (Fig. 5b) reveal similar electrochemical behavior of redox potential.

The results of CV studies conducted on the BSA/Ab-AFB_1/n-Sm_2O_3/ITO immunoelectrode obtained as a function of scan

Published on 03 July 2013. Downloaded by Korea Institute of Science and Technology / KIST on 30/07/2013 02:23:21.

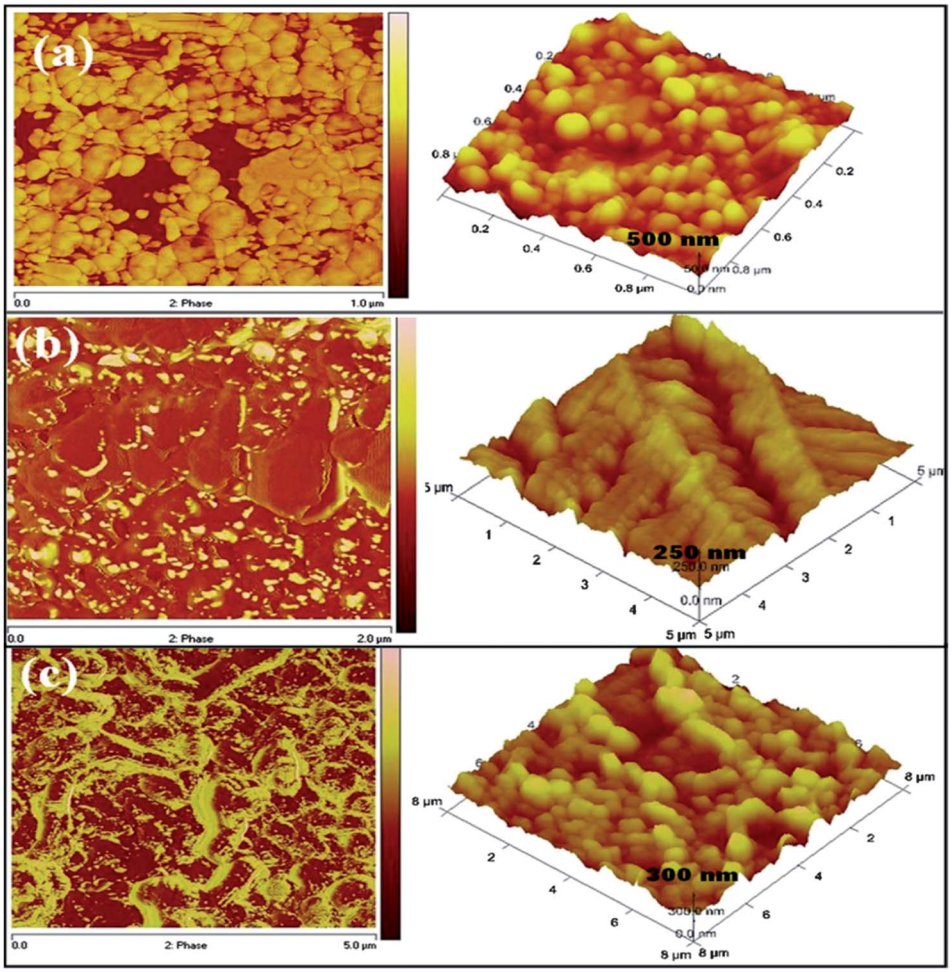

Fig. 4 Two dimensional and three dimensional AFM micrographs of (a) n-Sm_2O_3/ITO, (b) Ab-AFB_1/n-Sm_2O_3/ITO electrode and (c) BSA/Ab-AFB_1/n-Sm_2O_3/ITO immunoelectrode.

rate varying from 10 to 100 mV s^{-1} are shown in Fig. 5c. It is observed that magnitudes of both anodic (I_{pa}) and cathodic (I_{pc}) peak currents increase linearly with square root of the scan rate ($v^{1/2}$) (Fig. 5d), suggesting that electrochemical reaction is a diffusion-controlled process. The anodic (E_{pa}) and cathodic (E_{pc}) peak potentials and potential peak shifts ($\Delta E_p = E_{pa} - E_{pc}$) exhibit a linear relationship (linear regression coefficient 0.9833) with a scan rate indicating facile charge transfer kinetics in the 10–100 mV s^{-1} range of the scan rate shown in Fig. S3 in the ESI†. These results reveal that the n-Sm_2O_3/ITO electrode can be used for the immobilization of Ab-AFB_1, providing sufficient accessibility to electrons to shuttle between the antibodies and the electrode. The diffusion co-efficient (D) value of the redox species from the electrolyte to the BSA/Ab-AFB_1/n-Sm_2O_3/ITO immunoelectrode has been calculated using the Randles–Sevcik equation.[37]

$$I_p = (2.69 \times 10^5) n^{3/2} A D^{1/2} C v^{1/2} \quad \text{(v)}$$

where I_p is the peak current of the immunoelectrode (I_{pa} anodic and I_{pc} cathodic), n is the number of electrons involved or electron stoichiometry (1), A is the surface area of the immunoelectrode (0.25 cm^2), D is the diffusion co-efficient, C is the concentration of redox species (5 mM $[Fe(CN)_6]^{3-/4-}$) and v is the scan rate (20 mV s^{-1}). The D value has been obtained to be 2.26×10^{-5} cm^2 s^{-1}.

The surface concentration of the BSA/Ab-AFB_1/n-Sm_2O_3/ITO immunoelectrode can be estimated from the plot of current *versus* potential (CV) using the Brown-Anson model,[26] *via* the following equation.

$$I_p = n^2 F^2 \gamma A v / 4RT \quad \text{(vi)}$$

where n is the number of electrons transferred (1), F is the Faraday constant (96 485 C mol^{-1}), γ is the surface concentration of the corresponding electrode (mol cm^{-2}), A is the surface area of the electrode (0.25 cm^2), v is the scan rate (20 mV s^{-1}), R is the gas constant (8.314 J mol^{-1} K^{-1}) and T is room temperature (25 °C). The surface concentration of Ab-AFB_1/n-Sm_2O_3/ITO (8.08×10^{-11} mol cm^{-2}) is higher than that of the BSA/Ab-AFB_1/n-Sm_2O_3/ITO (4.83×10^{-11} mol cm^{-2}), n-Sm_2O_3/ITO (6.02×10^{-11} mol cm^{-2}) and ITO (4.01×10^{-11} mol cm^{-2}) electrodes.

The value of the heterogeneous electron transfer rate constant (K_s) obtained for the BSA/Ab-AFB_1/n-Sm_2O_3/ITO

 This journal is © The Royal Society of Chemistry 2013

Published on 03 July 2013. Downloaded by Korea Institute of Science and Technology / KIST on 30/07/2013 02:23:21.

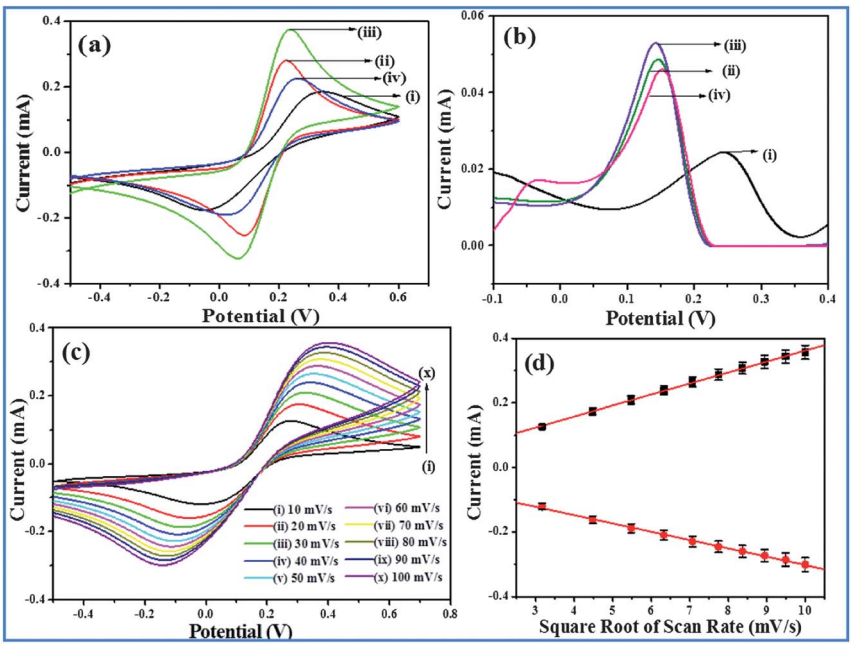

Fig. 5 (a) Cyclic voltammogram and (b) differential pulse voltammogram of bare ITO (i), n-Sm_2O_3/ITO (ii), Ab-AFB_1/n-Sm_2O_3/ITO (iii) and BSA/Ab-AFB_1/n-Sm_2O_3/ITO immunoelectrode (iv). (c) CV of the BSA/Ab-AFB_1/n-Sm_2O_3/ITO immunoelectrode with increasing scan rate from 10 to 100 mV s^{-1}. (d) The magnitude of current *vs.* potential difference as a function of square root of scan rate (10–100 mV s^{-1}) measured in PBS (50 mM, pH 6.0, 0.9% NaCl) containing $[Fe(CN)_6]^{3-/4-}$ (5 mM) at 20 mV s^{-1} scan rate in the potential range of −0.3 V to 0.6 V.

immunoelectrode has been calculated from the Lavrion model:[38]

$$K_s = mnFv/RT \quad \text{(vii)}$$

where m is the peak-to-peak separation (0.23 V), F is the Faraday constant (96 485 C mol^{-1}), v is the scan rate (20 mV s^{-1}), n is the number of transferred electrons (2), R is the gas constant (8.314 J mol^{-1} K^{-1}) and T is room temperature (25 °C). The value of K_s is found to be 0.36 s^{-1}, which indicates fast electron transfer between the immobilized antibodies and electrode due to the presence of Sm_2O_3 nanoparticles.

4.5 Electrochemical impedance spectroscopy (EIS) studies

The electrochemical impedance spectroscopy studies have been carried out to measure the impedance change of the electrode surface as a result of the modification process. In EIS, the semicircular diameter of the EIS spectra yields a value of the charge transfer resistance (R_{CT}) that reveals electron transfer kinetics of the redox probe at the electrode–electrolyte interface. The linear part of the low-frequency region corresponds to the diffusion process. Fig. 6a shows the EIS spectra of bare ITO, n-Sm_2O_3/ITO, Ab-AFB_1/n-Sm_2O_3/ITO and BSA/Ab-AFB_1/n-Sm_2O_3/ITO immunoelectrode, where R_{CT} is the charge transfer resistance of the electrode and electrolyte interface in PBS (50 mM, pH 6.0, 0.9% NaCl) containing $[Fe(CN)_6]^{3-/4-}$ (5 mM). The EIS spectra have been recorded in the frequency range, 0.1–10^7 Hz with perturbation amplitude of 0.05 V. Under the open circuit condition, the magnitude of DC potential is 0 mV with 5 data points per frequency decade is used during measurements of EIS spectra. As shown in the Nyquist plot, an R_{CT} value of n-Sm_2O_3/ITO (R_{CT} = 2.11 kΩ, curve ii) is smaller than that of the bare ITO electrode (R_{CT} = 5.21 kΩ, curve i). This suggests that the n-Sm_2O_3 film results in improved conductivity of the electrode and the positively charged Sm^{3+} ions facilitate diffusion of the negatively charged $[Fe(CN)_6]^{3-/4-}$ ions towards the electrode surface. The R_{CT} value further decreases for the Ab-AFB_1/n-Sm_2O_3/ITO electrode (R_{CT} = 1.55 kΩ, curve iii) after immobilization of the AFB_1 antibodies indicating that non-binding sites on Ab-AFB_1 promote electron transfer between the Ab-AFB_1/n-Sm_2O_3/ITO electrode and the electrolyte. Moreover, after the immobilization of BSA onto the Ab-AFB_1/n-Sm_2O_3/ITO electrode, significant enhancement in R_{CT} (3.06 kΩ, curve iv) is observed. This may be due to insulating nature of the BSA layer that perhaps hinders diffusion of ferricyanide ions toward the electrode surface resulting in an increased value of R_{CT}. The observed change in R_{CT} after BSA immobilization can be assigned to the dielectric and insulating features at the electrode–electrolyte interface indicating immobilization of antibodies.

$$R_{CT}(c) < R_{CT}(b) < R_{CT}(d) < R_{CT}(a) \quad \text{(viii)}$$

4.6 Effect of pH

Evaluation of a suitable pH for the buffer solution is very important since it may influence electrochemical behavior of the BSA/Ab-AFB_1/n-Sm_2O_3/ITO immunoelectrode because activity of the immobilized antibody is known to be pH dependent. The effect of solution pH (in the range of 5.5 to 8.0) on the BSA/Ab-AFB_1/n-Sm_2O_3/ITO immunoelectrode has been investigated by the CV technique (Fig. 6b) in PBS (50 mM, 0.9% NaCl) containing $[Fe(CN)_6]^{3-/4-}$ (5 mM) at 20 mV s^{-1} scan rate.

Published on 03 July 2013. Downloaded by Korea Institute of Science and Technology / KIST on 30/07/2013 02:23:21.

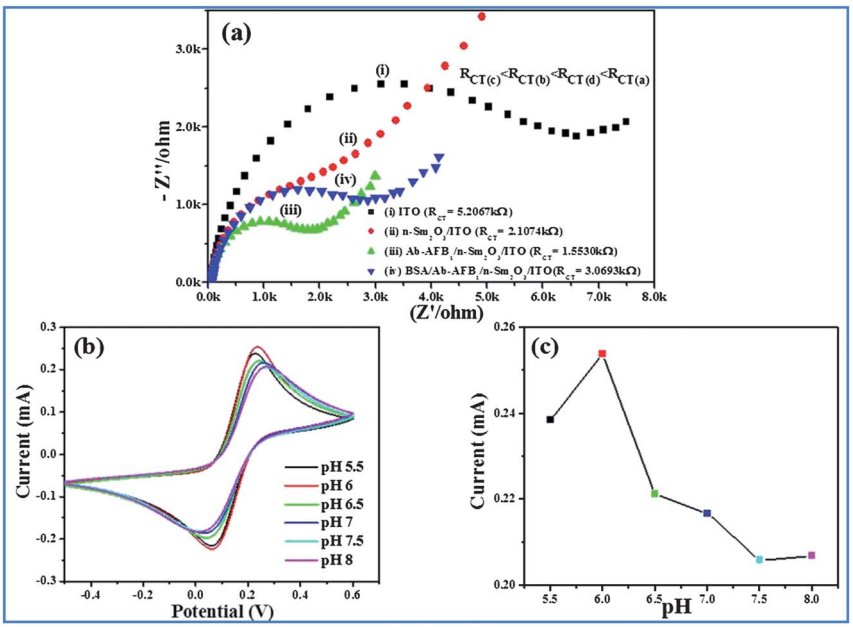

Fig. 6 (a) Electrochemical impedance spectra of bare ITO (i), n-Sm_2O_3/ITO (ii), Ab-AFB_1/n-Sm_2O_3/ITO (iii) and BSA/Ab-AFB_1/n-Sm_2O_3/ITO immunoelectrode (iv). (b) CV studies and (c) conjugative change in current response of the BSA/Ab-AFB_1/n-Sm_2O_3/ITO immunoelectrode as a function of pH (ranging from 5.5 to 8) in PBS (50 mM, 0.9% NaCl) containing $[Fe(CN)_6]^{3-/4-}$ (5 mM).

As seen in Fig. 6c the oxidation peak current increases from pH 5.0 to 6.0 and the highest magnitude of peak current is obtained at pH 6.0. When pH further increases, the oxidation peak current decreases gradually and the potential peak shifts to higher values. This may be attributed to non-availability of the positively charged moieties (Sm^{+3}) present on the matrix as the pH of the solution approaches its isoelectric point resulting in decreased interaction between $[Fe(CN)_6]^{3-/4-}$ ions on the n-Sm_2O_3 surface and also for loss of the activity of immobilized antibodies at elevated pH. This result suggests that the BSA/Ab-AFB_1/n-Sm_2O_3/ITO immunoelectrode is most active at pH 6.0 for AFB_1 detection and at this pH, Ab-AFB_1 and BSA retain their natural structures and do not denature. Moreover, it appears that higher pH is responsible for desorption of the biomolecule, and the current response decreases by ~19% at pH < 8.0. Thus all the experiments have been conducted at pH 6.0. The results of electrochemical measurements have been carried out in triplet sets under identical conditions revealing good reproducibility.

4.7 Electrochemical response studies of the BSA/Ab-AFB_1/n-Sm_2O_3/ITO immunosensor

The electrochemical response studies (Fig. 7a) of the BSA/Ab-AFB_1/n-Sm_2O_3/ITO immunoelectrode have been performed as a function of AFB_1 concentration (0–700 pg mL^{-1}) in PBS (50 mM, pH 6.0, 0.9% NaCl) containing $[Fe(CN)_6]^{3-/4-}$ (5 mM) at 20 mV s^{-1} scan rate using the CV technique. The oxidation peaks are obtained around 0.3 V corresponding to the biochemical reaction between Ab-AFB_1 and AFB_1. The magnitude of peak current is found to increase on successive addition of AFB_1. This is assigned to the formation of an antigen–antibody complex between AFB_1 and Ab-AFB_1 on the electrode surface that acts as an electron transfer accelerating layer for transfer of electrons. The corresponding calibration curve (Fig. 7b) shows that the magnitude of peak current increases almost linearly with increasing AFB_1 concentration and saturates at higher concentration of AFB_1. However, under optimized conditions the modified BSA/Ab-AFB_1/n-Sm_2O_3/ITO immunoelectrode shows good linearity to AFB_1 in the broad concentration range, 10–700 pg mL^{-1} with a linear regression co-efficient of 0.961. The sensitivity of the fabricated immunoelectrode calculated from the slope of the curve is found to be 48.39 μA pg^{-1} mL^{-1} cm^{-2}. The standard deviation and low detection limit for the immunoelectrode are obtained to be 9.329 μA and 57.82 pg mL^{-1} cm^{-2}, respectively.

The association constant (K_a) for the BSA/Ab-AFB_1/n-Sm_2O_3/ITO immunoelectrode, estimated from the Hanes plot *i.e.*, the graph between [substrate concentration] and [substrate concentration/current] (Fig. 7c), has been found to be 47.9 pg mL^{-1}. The value of K_a depends on various factors such as the matrix and the method of immobilization of antibodies that could bring different conformational changes in the antibody structure. The small K_a value indicates increased affinity of the immobilized antibodies of the BSA/Ab-AFB_1/n-Sm_2O_3/ITO immunoelectrode to the antigen that can be attributed to favorable conformation of Ab-AFB_1 and higher loading onto the n-Sm_2O_3/ITO electrode surface.

4.8 Thermal stability, response time, reproducibility, interferences and shelf-life of the BSA/Ab-AFB_1/n-Sm_2O_3/ITO immunoelectrode

The current response of the fabricated BSA/Ab-AFB_1/n-Sm_2O_3/ITO immunoelectrode as a function of temperature (in the

 This journal is © The Royal Society of Chemistry 2013

Published on 03 July 2013. Downloaded by Korea Institute of Science and Technology / KIST on 30/07/2013 02:23:21.

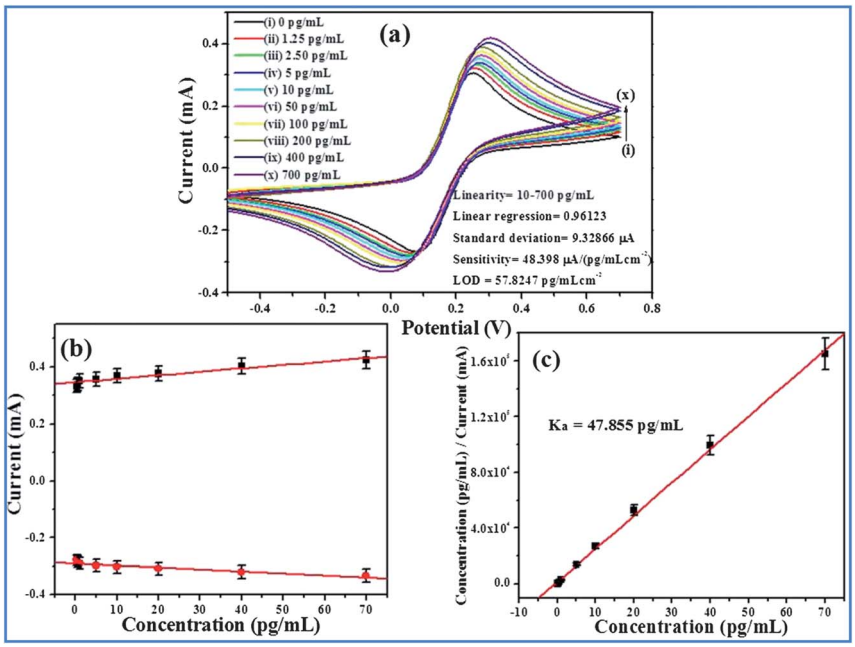

Fig. 7 (a) Electrochemical response study of the BSA/Ab-AFB_1/n-Sm_2O_3/ITO immunoelectrode with respect to the AFB_1 concentration (0–700 pg mL^{-1}) in PBS (50 mM, pH 6.0, 0.9% NaCl) containing $[Fe(CN)_6]^{3-/4-}$ (5 mM). (b) Calibration curve and the variation in current as a function of AFB_1 concentration. (c) Hanes plot, which plots the substrate concentration (*X*-axis) and substrate concentration/current (*Y*-axis).

range of 15–60 °C) has been investigated by the CV technique in PBS (50 mM, pH 6.0, 0.9% NaCl) containing $[Fe(CN)_6]^{3-/4-}$ (5 mM) at 20 mV s^{-1} scan rate. It can be seen (Fig. 8b) that the amperometric current response increases linearly up to 50 °C after which it shows a sharp decrease, indicating that the immobilized biomolecules get denatured after 50 °C. These results suggest that antibodies bioconjugated with n-Sm_2O_3 nanorods are thermally stable.

The response time of the BSA/Ab-AFB_1/n-Sm_2O_3/ITO immunoelectrode has been determined by measuring amperometric current response by varying the incubation period from 2 to 60 s (Fig. 8a). This biosensor achieves 95% of the steady-state current

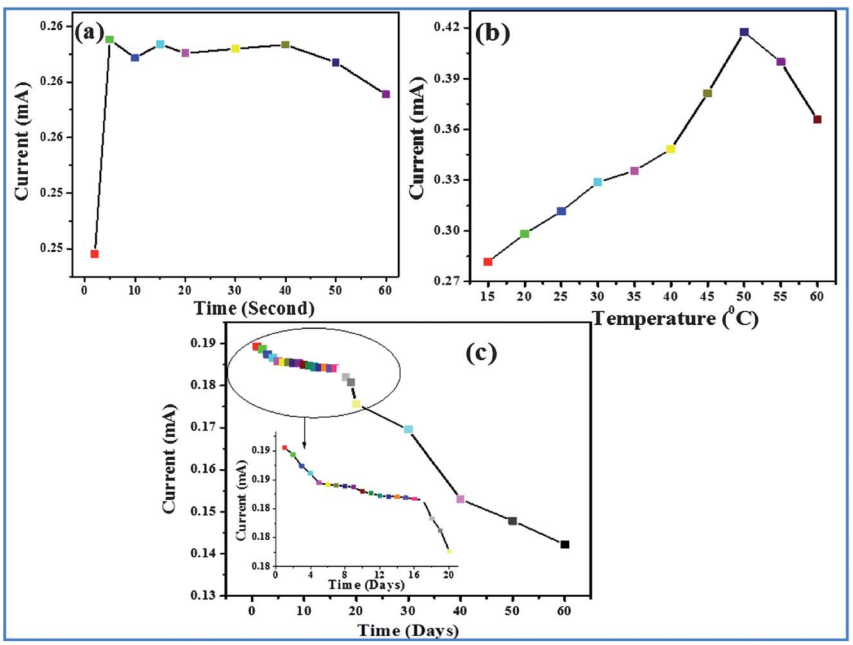

Fig. 8 (a) Electrochemical response time of the BSA/Ab-AFB_1/n-Sm_2O_3/ITO immunoelectrode from 2 to 60 s incubation period. (b) Effect of temperature on the BSA/Ab-AFB_1/n-Sm_2O_3/ITO immunoelectrode from 15 to 60 °C. (c) Shelf-life curve for the BSA/Ab-AFB_1/n-Sm_2O_3/ITO immunoelectrode as a function of days.

Published on 03 July 2013. Downloaded by Korea Institute of Science and Technology / KIST on 30/07/2013 02:23:21.

Table 1 Characteristics of the BSA/Ab-AFB$_1$/n-Sm_2O_3/ITO bioelectrode along with those reported in the literature for aflatoxin B$_1$ detection, with their important parameters

SN	Bioelectrode	Detection range (pg mL^{-1})	Detection limit (pg mL^{-1})	Sensitivity	K_a value	Response time (s)	Shelf-life (days)	Ref.
1	BSA-anti-AFB$_1$/Au NPs	500–10 000	100	1.4 μS ng^{-1} mL^{-1}	—	—	12	23
2	HRP-anti-AFB$_1$/nano Au/TiO_2/RTIL/Nafion/GCE	100–12 000	50	0.12 μA ng^{-1} mL^{-1}	—	—	19	24
3	BSA/a-AfB$_1$/DMSO/ RnNi-film/ITO	50–1000	327	0.59 μA ng^{-1} dL^{-1}	1.3 × 10^{14} mol L^{-1}	5	60	26
4	BSA-anti-AFB$_1$/RGO/ITO	125–1500	150	68 μA ng^{-1} mL^{-1}	5 × 10^{-4} ng mL^{-1}	—	45	27
5	AFO/MWCNTs/Pt	1000–225 000	500	1.06 nA ng^{-1} dL^{-1}	7.03 μM L^{-1}	44	23	29
6	BSA/aAFB$_1$-*C*-AuNP/MBA/Au	100–1000	179	0.45 μA ng^{-1} dL^{-1}	—	60	—	39
7	BSA-anti-AFB$_1$/AuNps/ PTH-GCE	600–2400	70	1.23 μA ng^{-1} mL^{-1}	—	—	—	40
8	BSA/Ab-AFB$_1$/n-Sm_2O_3/ITO	10–700	57.82 pg mL^{-1} cm^{-2}	48.39 μA pg^{-1} mL^{-1} cm^{-2}	47.9 pg mL^{-1}	5	60	Present work

in less than 5 s revealing fast electron exchange between the immobilized antibodies and the n-Sm_2O_3/ITO electrode. After 5 s, the current response becomes almost constant indicating that 5 s is the response time of the fabricated immunoelectrode.

The interference studies of this immunosensor have been investigated in the presence of another food toxin namely ochratoxin-A (10.0 pg mL^{-1}) using CV (see Fig. S4 in the ESI†). There is no significant change in the current response as evident by the observed very low relative standard deviation (0.39%) indicating that this immunosensor is highly selective for this particular food toxin.

The shelf-life of the BSA/Ab-AFB$_1$/n-Sm_2O_3/ITO immunoelectrode (Fig. 8c) has been evaluated by measuring amperometric current response in the presence of 100 pg mL^{-1} standard AFB$_1$ solution in PBS (50 mM, pH 6.0, 0.9% NaCl) at a regular interval of 1 day up to 20 days and then after a gap of 10 days. It has been found that the fabricated immunoelectrode retains its activity up to 94% after 20 days, 89% after 30 days, 84% after 40 days and falls to 73% after 60 days when stored under refrigerated conditions (4 °C). The reproducibility of the proposed immunosensor has been estimated by repetitive measurement of current response with 100 pg mL^{-1} standard AFB$_1$ solutions in PBS. The results obtained in 15 repeated measurements show an RSD of 2–3%, indicating that the obtained data are reproducible. The sensing characteristics of the BSA/Ab-AFB$_1$/n-Sm_2O_3/ITO immunosensor are summarized in Table 1 along with those reported in the literature.[23,24,26,27,29,39,40]

5 Conclusions

This work describes an electrochemical immunosensor with Sm_2O_3 nanorod modification for food toxin (AFB$_1$) detection. It has been demonstrated that the electrophoretically deposited n-Sm_2O_3 film can be used for immobilization of the Ab-AFB$_1$ and BSA for blocking non-specific binding sites of Ab-AFB$_1$ to detect aflatoxins. The results of electrochemical studies conducted on fabricated BSA/Ab-AFB$_1$/n-Sm_2O_3/ITO immunoelectrode show a high sensitivity of 48.39 μA pg^{-1} mL^{-1} cm^{-2}, broad linear range (10–700 pg^{-1} mL^{-1}), low detection limit of 57.82 pg^{-1} mL^{-1} cm^{-2}, and fast response time of 5 s. Moreover, the superior sensing performance of this immunoelectrode has been combined with high thermal stability, good reproducibility and long-term stability. These studies have revealed a new promising platform for the application of rare earth metal oxide materials that have implications in clinical diagnostics, antibody screening and proteomics research.

Acknowledgements

This study was supported by World Class University (WCU) program (R31-20029) through the National Research Foundation (NRF) funded by the Ministry of Education, Science, and Technology (MEST), Republic of Korea. We acknowledge the financial support received under the Indian Council of Medical Research project [ICMR(RHN/ADHOC/5/2012-2013)] and Department of Science & Technology project [DST/TSG/ME/2008/18] and the in-house NPL project (OLP-070632D). J.S. is thankful to National Physical Laboratory, New Delhi, India for providing the facilities and Council of Scientific & Industrial Research (CSIR) India for the award of a Research Associateship during 2010–2012. A. R. sincerely acknowledges Indian Council of Medical Research (ICMR), New Delhi, for the award of a Project Associateship. B. D. M. thanks the Ministry of Education, Science and Technology (R32−20026) of Korea for the opportunity provided during his visit to the Chungnam National University as a visiting professor under the World Class University project during 2013.

Notes and references

1 A. Kaushik, P. R. Solanki, A. A. Ansari, S. Ahmad and B. D. Malhotra, *Nanotechnology*, 2009, **20**, 055105–055113.
2 M. H. Wu, T. W. Lin, M. D. Huang, H. Y. Wang and T. M. Pan, *Sens. Actuators, B*, 2010, **146**, 342–348.
3 M. Guo, J. Lu, Y. Wu, Y. Wang and M. Luo, *Langmuir*, 2011, **27**, 3872–3877.
4 Y. Li, Y. Gao, Y. Zhou, Y. Liu and J. Liu, *J. Electroanal. Chem.*, 2010, **642**, 1–5.

 This journal is © The Royal Society of Chemistry 2013

Published on 03 July 2013. Downloaded by Korea Institute of Science and Technology / KIST on 30/07/2013 02:23:21.

5 L. Eyring, in *The Handbook on the Physics and Chemistry of Rare Earths*, ed. K. A. Gschneider Jr and L. Eyring, North Holland, Amsterdam, 1979.
6 A. Rosengren and B. Johansson, *Phys. Rev. B*, 1982, **26**, 3068–3078.
7 I. Gur, N. A. Fromer, M. L. Geier and A. P. Alivisatos, *Science*, 2005, **310**, 462–465.
8 M. S. Gudiksen, L. J. Lauhon, J. Wang, D. C. Smith and C. M. Lieber, *Nature*, 2002, **415**, 617–620.
9 H. Yang, H. Wang, H. M. Luo, D. M. Feldmann, P. C. Dowden, R. F. DePaula and Q. X. Jia, *Appl. Phys. Lett.*, 2008, **92**, 062905.
10 T. M. Pan, M. D. Huang, W. Y. Lin and M. H. Wu, *Anal. Chim. Acta*, 2010, **669**, 68–74.
11 O. Engstrom, B. Raeissi, S. Hall, O. Buiub, M. C. Lemmec, H. D. B. Gottlob, P. K. Hurley and K. Cherkaoui, *Solid-State Electron.*, 2007, **51**, 622–626.
12 Z. Jiang, W. Zhou, D. Tan, R. Zhai and X. Bao, *Surf. Sci.*, 2004, **565**, 269–278.
13 M. H. Wu, C. H. Cheng, C. S. Lai and T. M. Pan, *Sens. Actuators, B*, 2009, **138**, 221–227.
14 S. S. Hosseini and R. Bagher, *Intl. J. Agron. Plant Prod.*, 2012, **3**, 179–184.
15 K. C. Ehrlich, B. G. Montalbano and P. J. Cotty, *Fungal Genet. Biol.*, 2003, **38**, 63–74.
16 International Agency for Research on Cancer, *IARC Monographs on the Evaluations of Carcinogenic Risks to Human*, IARC, Lyon, 1993, vol. 56, pp. 489–521.
17 J. D. Thrasher and S. L. Crawley, *Toxicol. Ind. Health*, 2009, **25**, 583–616.
18 G. Cortés, M. Carvajal, I. Méndez-Ramírez, E. Avila-González, N. Chilpa-Galván, P. Castillo-Urueta and C. M. Flores, *Poult. Sci.*, 2010, **89**(5), 993–1001.
19 A. Fernandez, R. Belio, J. J. Ramos, M. C. Sanz and T. Saez, *J. Sci. Food Agric.*, 1997, **74**, 161–168.
20 E. Chiavaro, C. Dall'Asta, G. Galaverna, A. Biancardi, E. Gambarelli, A. Dossena and R. Marchelli, *J. Chromatogr., A*, 2001, **937**, 31–40.
21 W. B. Shim, J. G. Choi, J. Y. Kim, Z. Y. Yang, K. H. Lee, M. G. Kim and S. D. Ha, *J. Food Prot.*, 2008, **71**, 781–789.
22 A. Y. Kolosova, W. B. Shim, Z. Y. Yang, S. A. Eremin and D. H. Chung, *Anal. Bioanal. Chem.*, 2005, **384**, 286–294.
23 Y. Liu, Z. Qin, X. Wu and H. Jiang, *Biochem. Eng. J.*, 2006, **32**, 211–217.
24 A.-L. Sun, Q.-A. Qi, Z.-L. Dong and K. Z. Liang, *Sens. Instrum. Food Qual. Saf.*, 2008, **2**, 43–50.
25 Z. Linting, L. Ruiyi, L. Zaijun, X. Qianfang, F. Yinjun and L. Junkang, *Sens. Actuators, B*, 2012, **174**, 359–365.
26 P. Kalita, J. Singh, M. K. Singh, P. R. Solanki, G. Sumana and B. D. Malhotra, *Appl. Phys. Lett.*, 2012, **100**, 093702–093705.
27 S. Srivastava, V. Kumar, M. A. Ali, P. R. Solanki, A. Srivastava, G. Sumana, P. S. Saxena, A. G. Joshi and B. D. Malhotra, *Nanoscale*, 2013, **5**, 3043–3051.
28 D. Zhang, P. Li, Q. Zhang and W. Zhang, *Biosens. Bioelectron.*, 2011, **26**, 2877–2882.
29 S. C. Li, J. H. Chen, H. Cao, D. S. Yao and D. L. Liu, *Food Control*, 2011, **22**, 43–49.
30 S. Wu, N. Duan, C. Zhu, X. Ma, M. Wang and Z. Wang, *Biosens. Bioelectron.*, 2011, **30**, 35–42.
31 Y. S. Zhao, H. Fu, A. Peng, Y. Ma, Q. Liao and J. Yao, *Acc. Chem. Res.*, 2010, **43**, 409–418.
32 T. D. Nguyen, D. Mrabet and T. O. Do, *J. Phys. Chem. C*, 2008, **112**, 15226–15235.
33 U. Yogeswaran and S. M. Chen, *Sensors*, 2008, **8**, 290–313.
34 Z. P. Wei, M. Arredondo, H. Y. Peng, Z. Zhang, D. L. Guo, G. Z. Xing, Y. F. Li, L. M. Wong, S. J. Wang, N. Valanoor and T. Wu, *ACS Nano*, 2010, **4**, 4785–4791.
35 J. Singh, M. Srivastava, A. Roychoudhury, D. W. Lee, S. H. Lee and B. D. Malhotra, *J. Phys. Chem. B*, 2013, **117**, 141–152.
36 L. Besra and M. Liu, *Prog. Mater. Sci.*, 2007, **52**, 1–61.
37 J. Singh, M. Srivastava, P. Kalita and B. D. Malhotra, *Process Biochem.*, 2012, **47**, 2189–2198.
38 J. Singh, P. Kalita, M. K. Singh and B. D. Malhotra, *Appl. Phys. Lett.*, 2011, **98**, 123702.
39 A. Sharma, Z. Matharu, G. Sumana, P. R. Solanki, C. G. Kim and B. D. Malhotra, *Thin Solid Films*, 2010, **519**, 1213–1218.
40 J. Owino, O. Arotiba, N. Hendricks, E. A. Songa, N. Jahed, T. Waryo, R. Ngece, P. Baker and E. Iwuoha, *Sensors*, 2008, **8**, 8262–8274.